A scalar Poincaré map for anti-phase bursting in coupled inhibitory neurons with synaptic depression.

Mark Olenik [1,*], and Conor Houghton [2]

[1]School of Biological Sciences, Faculty of Life Sciences, University of Bristol, Bristol, United Kingdom
[2]School of Computer Science, Electrical and Electronic Engineering, and Engineering Mathematics, Faculty of Engineering, University of Bristol, Bristol, United Kingdom

Correspondence*:
Mark Olenik
m.olenik@bristol.ac.uk

2 ABSTRACT

Short-term synaptic plasticity is found in many areas of the central nervous system. In the inhibitory half-centre central pattern generators involved in locomotion, synaptic depression is believed to act as a burst termination mechanism, allowing networks to generate anti-phase bursting patterns of varying periods. To better understand burst generation in these central patter generators, we study a minimal network of two neurons coupled through depressing synapses. Depending on the strength of the synaptic conductance between the two neurons, this network can produce symmetric $n : n$ anti-phase bursts, where neurons fire n spikes in alternation, with the period of such solutions increasing with the strength of the synaptic conductance. Relying on the timescale disparity in the model, we reduce the eight-dimensional network equations to a fully-explicit scalar Poincaré burst map. This map tracks the state of synaptic depression from one burst to the next and captures the complex bursting dynamics of the network. Fixed points of this map are associated with stable burst solutions of the full network model, and are created through fold bifurcations of maps. We derive conditions that describe period-increment bifurcations between stable $n : n$ and $(n + 1) : (n + 1)$ bursts, producing a full bifurcation diagram of the burst cycle period. Predictions of the Poincaré map fit excellently with numerical simulations of the full network model and allow the study of parameter sensitivity for rhythm generation.

Keywords: Synaptic depression, Poincaré map, Dynamical system, Neuronal bursting, Central pattern generator

1 INTRODUCTION

Short-term synaptic plasticity may have a role in burst activity in central pattern generators (CPGs). Short-term synaptic depression is commonly found in neuronal networks involved in the generation of rhythmic movements, such as in the pyloric CPG of the spiny lobster [1, 2], or in the lumbosacral cord of the chick embryo [3]. Synaptic depression modulates the strength of synapses in response to changes to the presynaptic firing frequency. At a high neuronal firing frequency, depression weakens the strength of synapses and therefore reduces the magnitude of the postsynaptic response. At low firing frequency, it allows sufficient time for the synapse to recover from depression between spikes, leading to a stronger postsynaptic response. In reciprocal networks, synaptic depression has been shown to act as a "switch", giving rise to a wide range of network dynamics such as synchronous and multi-stable rhythms, as well as fine tuning the frequency of network oscillations [4, 5, 6].

Brown [7] pioneered the idea that synaptic depression acts as a burst termination mechanism in reciprocally inhibitory CPGs involved in rhythm generation of locomotion. When one side is firing during a burst the other, antagonistic side, is prevented from firing by synaptic inhibition. However, the weakening of inhibition as a result of synaptic depression eventually releases the antagonistic side so that it starts firing, terminating the burst on the side that had originally been firing. This rhythmogenesis hypothesis has been considered one of a handful of standard mechanisms for

generating locomotion rhythms in vertebrates [8, 9, 10]. It has been proposed as an explaination of the antiphase burst rhythm in struggling in Xenopus tadpoles [11].

Bose and Booth [6] investigated burst generation in a generic half-centre CPG that consists of two identical, tonically active Morris-Lecar [12] neurons coupled through inhibitory depressing synapses. Numerical simulations showed that when the reciprocal synaptic conductance between the two neurons is varied, the network produces symmetric $n : n$ anti-phase bursts, with stronger synaptic coupling leading to longer bursts. They used methods from geometric singular perturbation theory to separate the timescales of the fast membrane, and the slow synaptic dynamics of the network to derive one-dimensional conditions necessary for the existence of stable $n : n$ solutions (for $n \leq 2$). According to these conditions the type of firing pattern largely depends on the slow depression dynamics of the synapses between the two neurons, and can therefore be predicted by knowing the strengths of the synaptic conductances of the two synapses. Thus, the scalar conditions derived in Bose and Booth [6] provide a method to numerically identify the type of stable $n : n$ pattern for any given value of the coupling strength. However, they do not predict the exact period of such solutions. Furthermore, while they provide good arguments for the validity of their reduction assumptions and the resulting scalar conditions, they do not verify them numerically.

Here we extend the previous analysis by providing a Poincaré map of the slow depression dynamics. This allows us not only to predict the types of stable $n : n$ solutions the full network can produce, (for any n), but also to study how varying the coupling strength affects the period of such solutions. To do this, we build on, and numerically test, the assumptions on the fast-slow timescale disparity made in [6]. We reduce the two-cell model to a scalar Poincaré map that tracks the evolution of the depression from the beginning of one burst to the beginning of the next burst. Stable fixed points of our map are associated with stable $n : n$ burst solutions. Our map construction is motivated by the burst length map of a T-type calcium current, utilised by Matveev et al. [13], which approximates the anti-phase bursting dynamics of a network of two coupled Morris-Lecar neurons. In contrast to our model, the network described in the [13] paper does not contain short-term synaptic depression, and burst termination is instead accomplished through the dynamics of a slow T-type calcium current.

The Poincaré map derived here replicates the results from numerical simulations of the full two-cell ODE system: Given the strength of maximum conductance between the two neurons, fixed points of our map predict the type and period of $n : n$ patterns, the switch between burst solutions of different periods, as well as the occurrence of co-existent solutions. In addition to proving the existence and stability of fixed points, our map shows that fixed points are created via a fold bifurcation of maps. We also derive algebraic conditions that predict the period increment bifurcations that allow the switch between $n : n$ and $(n + 1) : (n + 1)$ solutions. Because our map is fully explicit, it lays the framework for studying the effects of other model parameter on network dynamics without the need to run expensive numerical integrations of the ODEs.

This paper is organised as follows. First, we introduce the network of two neurons, and describe the properties of single cell and synapse dynamics. We use numerical simulations of the network to provide an intuition for the range of possible burst dynamics the system can produce. Next, we state and justify the simplifying assumptions that are necessary for the map construction. Finally, we analytically derive the first return map of the depression variable as well as the conditions that are required for stable solutions to bifurcate between $n : n$ and $(n + 1) : (n + 1)$ solutions. We end this work with a discussion.

2 MATERIALS AND METHODS

We consider a pair of identical Morris-Lecar neurons [12], with parameters adapted from [6]. The Morris-Lecar model is a set of two first-order differential equations that describe the membrane dynamics of a spiking neuron. The depolarisation is modelled by an instantaneous calcium current, and the hyperpolarisation by a slow potassium current and a leak current. The membrane potential

v_i and potassium activation w_i of neuron i ($i, j = 1, 2$) is described by:

$$\dot{v}_i = f(v_i, w_i) - \bar{g}s_j(v_i - v_s), \tag{1}$$

$$\dot{w}_i = h(v_i, w_i). \tag{2}$$

Here v_s is the inhibitory reversal potential, and $\bar{g}$ and s_j are the maximal synaptic conductance and the synaptic gating, respectively, constituting the total inhibitory conductance $\bar{g}s_j$ from neuron j to neuron i. Function $f(v_i, w_i)$ describes the membrane currents of a single cell:

$$f(v_i, w_i) = -g_{\text{Ca}}m_\infty(v_i)(v_i - v_{\text{Ca}}) - g_{\text{K}}w_i(v_i - v_{\text{K}}) - g_{\text{L}}(v_i - v_{\text{L}}) + I. \tag{3}$$

The currents include a constant current I, and three ionic currents: an instantaneous calcium current, a potassium current, and a leak current, with respective reversal potentials v_{Ca}, v_{K}, and v_{L}, as well as maximum conductances g_{Ca}, g_{K}, and g_{L}. The function $h(v_i, w_i)$ models the kinetics of the potassium gating variable w_i, and is given by

$$h(v_i, w_i) = \frac{w_\infty(v_i) - w_i}{\tau_w} . \tag{4}$$

The steady-state activation functions m_∞ and w_∞ as well as the default model parameters are described in the Supplementary Material S1.

The dynamics of the synaptic interactions between the neurons are governed by a synaptic gating variable s_i and a depression variable d_i:

$$\dot{d}_i = \begin{cases} (1 - d_i)/\tau_a & \text{if } v_i < v_\theta, \tag{5} \\ -d_i/\tau_b & \text{if } v_i > v_\theta, \tag{6} \end{cases}$$

$$\dot{s}_i = \begin{cases} -s_i/\tau_\kappa & \text{if } v_i < v_\theta, \tag{7} \\ 0 & \text{if } v_i > v_\theta. \tag{8} \end{cases}$$

Variable d_i describes a firing rate dependent depletion mechanism that governs the amount of depression acting on the synapse. The model is agnostic with respect to the exact mechanism of this depletion, be it pre- or post-synaptic. When the voltage of cell i is above firing threshold ($v_i > v_\theta$), variable d_i decays with time constant τ_b, and recovers with time constant τ_a when voltage is below firing threshold ($v_i < v_\theta$). Since the synaptic inhibition occurs on a much faster timescale than synaptic depression, we assume that s_i is instantaneously reset to d_i whenever v_i increases above v_θ, where it remains throughout $v_i > v_\theta$. Whenever $v_i < v_\theta$, the synaptic variable decays exponentially with time constant τ_κ. The equations for the depression model were adapted from the Bose et al. [14] model. These equations are a mathematically tractable simplification of the established phenomenological depression model previously described by Tsodyks and Markram [15].

When the total inhibitory conductance $g = \bar{g}s$ is constant, the membrane dynamics are determined by the cubic v-nullcline $v_\infty(v_i)$ and the sigmoid w-nullcline $w_\infty(v_i)$, satisfying $\dot{v}_i = 0$ and $\dot{w}_i = 0$, respectively. In case of no inhibition ($g = 0$), the two curves intersect near the local minimum of v_∞ to the left of v_θ (commonly referred to as "left knee" of v_∞), creating an unstable fixed point with a surrounding stable limit cycle of period $T = T_{act} + T_{inact}$ (fig. 1A). Here T_{act} is the amount of time the cell spends in the active state when $v > v_\theta$, while T_{inact} is the time it spends in the silent state when $v < v_\theta$. Trajectories along that limit cycle have the familiar shape of the action potential (fig. 1B). The trajectory of an action potential can be dissected into four phases: (1) a silent phase, (2) a jump up, (3) an active phase, and (4) a jump down [see e.g. 16]. During the silent phase the trajectory evolves along the left branch ($v_i < v_\theta$) of the cubic v-nullcline. Once the trajectory reaches the local minimum of v_∞, it "jumps up" to the right branch ($v_i > v_\theta$), crossing the firing threshold v_θ. During the active phase the trajectory then evolves along the right branch of the

113 cubic until it arrives at the local maximum, where it "jumps down" to the left branch commencing
114 a new cycle. In the case of a non-zero inhibition ($g > 0$) the location of v_∞ depends on the exact
115 value of g. Increasing g moves the cubic v_∞ with the ensuing unstable fixed point down w_∞ in the
116 $(v - w)$ -plane. When g is large enough, the fixed point moves past the left knee and becomes stable
117 via a subcritical Andoronov-Hopf bifurcation, attracting all previously periodic trajectories. In the
118 following section we will refer to the value of the total conductance at the bifurcation as g_{bif}.

119 The two-cell network model is numerically integrated using an adaptive step-size integrator for
120 stiff differential equations implemented with XPPAUT [17] and controlled through the Python
121 packages SciPy [18] and PyXPP [19]. The following mathematical analysis is performed on the
122 equations of a single cell. Unless required for clarity, we will therefore omit the subscripts i, j from
123 here on. It should be noted that [6] used $n - n$ to denote the stable bursts with n spikes, however,
124 here we use the $n : n$ notation for more clarity.

3   RESULTS

3.1   Anti-phase burst solutions

126 Short-term synaptic depression of inhibition in a half-centre oscillator acts as a burst termination
127 mechanism [7] and is known to produce $n : n$ anti-phase burst solutions of varying period. Such $n : n$
128 solutions consist of cells firing bursts of n spikes in alternation. Figure 2A shows the timecourse
129 of a typical $4 : 4$ burst. While one cell is firing a burst it provides an inhibitory conductance to
130 the other cell, preventing it from firing. Therefore, at any given moment one cell is spiking while
131 the other is inhibited. Consistent with Bose and Booth [6] we will refer to the currently firing cell
132 as "free" and we will call the inhibited cell "suppressed". Additionally, we will distinguish between
133 two phases of a $n : n$ solution: We will refer to the time interval when a cell is firing as the "free
134 phase", and we will call the remaining duration of a cycle, when a cell is not firing, the "suppressed
135 phase".

136 With each action potential of the free cell, short-term depression leads to a step-wise decrease
137 of d, and consequently of s (fig. 2B). If d depresses faster at spike time than it can recover in the
138 inter-spike-intervals (ISIs), the total synaptic conductance $\bar{g}s$ will eventually become sufficiently
139 small to allow for the suppressed cell to be released and start firing, thus inhibiting the previously
140 free cell. While a cell is suppressed its depression variable can recover. Once the suppressed cell
141 becomes free again its synaptic inhibition will be sufficient to terminate the burst of the previously
142 free cell and commence a new cycle. As previously demonstrated by Bose and Booth [6], in a two-
143 cell reciprocally inhibitory network with synaptic depression the coupling strength $\bar{g}$ determines
144 the type of $n : n$ solution. Increasing $\bar{g}$ produces higher $n : n$ burst solutions with more spikes per
145 burst and a longer cycle period. Figure 3 shows numerically stable $n : n$ solutions for varying values
146 of $\bar{g}$. For small values of $\bar{g}$ the network produces anti-phase spiking $1 : 1$ solutions. As $\bar{g}$ is increased
147 the network generates solutions of increasing n, that is $2 : 2$, $3 : 3$, and $4 : 4$. When $\bar{g}$ is sufficiently
148 large (bottom of fig. 3), one of the cells continuously spikes at its uncoupled period T while the
149 other cell remains fully suppressed. Depending on the initial conditions either of the two cells can
150 become the suppressed cell, which is why the suppressed solution is numerically bistable.

151 Branches of numerically stable $n : n$ solutions and their associated limit cycle period for varying
152 values of $\bar{g}$ are depicted in fig. 4A (see Supplementary Material S2 for algorithm description). Not
153 only do higher $n : n$ solutions branches require stronger coupling $\bar{g}$, but also within $n : n$ branches
154 the period increases with $\bar{g}$. In line with Bose and Booth [6] we find small overlaps between solution
155 branches indicating numerical bistability, for example such as between the $2 : 2$ and $3 : 3$ solution
156 branches. Branches of higher $n : n$ burst solutions occur on increasingly smaller intervals of $\bar{g}$, for
157 instance is the $\bar{g}$ interval of the $5 : 5$ branch shorter than that of the $4 : 4$ branch and so on.
158 The interval between the $5 : 5$ branch and the suppressed solution (region between dotted lines in
159 fig. 4A) not only contains even higher numerically stable $n : n$ solutions, such as $11 : 11$ bursts, but
160 also other non-symmetric $n : m$ solutions as well irregular, non-periodic solutions. However, the
161 analysis in the following sections will only be concerned with the numerically stable and symmetric
162 $n : n$ solutions.

3.2   Mathematical analysis of two-cell network

The goal of the following mathematical analysis is to reduce the complexity of the eight-dimensional system to some easily tractable quantity. As we will see later this quantity is the value of the depression variable d of either of the two cells. We will construct the solution of d in a piecewise manner from one spike to the next, first during the free phase, and then during the suppressed phase. This construction will require two assumptions about the membrane and synaptic dynamics. The first assumption states that during a burst the free cell fires at its uncoupled period T, which simplifies the construction of the solution of d. The second assumption states that once the inhibitory conductance acting on the suppressed cell drops below a critical threshold, the cell is immediately released and fires. The second assumption is necessary to predict the release time of the suppressed cell, which allows us to model the recovery of d during the suppressed phase. In other words, the second assumption requires that the release of the suppressed cell from inhibition depends only on the timecourse of the inhibition, and not on the membrane dynamics of the suppressed cell. Both assumptions can be observed in coupled relaxation-oscillator types of neurons such as the Morris-Lecar model we use, and will be numerically verified below. Both assumptions were first explored in [6] to derive algebraic conditions that guarantee the periodicity of the depression variable for different $n : n$ solutions. However here we will use these assumptions to construct a Poincaré map of d, which will provide a geometric intuition for the dynamics of the full two-cell network and its dependence on model parameters.

Our first assumption about the model states that the free cell fires at its uncoupled period T, that is, during the free phase of a burst we have $ISI = T$. Solution profiles in fig. 3 suggest that the ISIs are indeed approximately constant. We can further numerically confirm this observation by capturing the ISIs of the stable solutions from the bifurcation diagram in fig. 4A. In addition to ISIs, Figure 4B also shows inter-burst intervals (IBIs), which correspond to the time interval between the last spike of the burst and the full cycle period, and which lie in the suppressed phase of the burst. IBIs lie on multiple branches, each branch associated with a stable $n : n$ solution, and are monotonically increasing with $\bar{g}$. In contrast, ISIs are calculated from the spikes within the free phase and do not vary significantly with $\bar{g}$, but are approximately $ISI \approx T$, affirming our first assumption. Assuming $ISI = T$ allows us to ignore the non-linear membrane dynamics during the free phase, and to construct the evolution of the synaptic variables iteratively from spike to spike. Assuming $ISI = T$ seems reasonable given that inhibition acting on the suppressed cell decays exponentially to zero on a much shorter timescale than the duration of the ISI, and therefore, once the suppressed cell is released its trajectory quickly approaches the spiking limit cycle.

Our second assumption states that the suppressed cell is released and spikes as soon as the total inhibitory conductance $g = \bar{g}s$ acting on it drops below a constant threshold. We call this critical threshold value the "release conductance", denoted by $g^\star$, and define it as the value of g at the time when the voltage of the suppressed cell first crosses the firing threshold v_θ, that is when that cell is released and fires its first spike. Recall from figure ... that when a cell is suppressed its v- and w-nullclines intersect at a stable fixed point and $g > g_{bif}$. A sufficient condition for the suppressed cell to be released is therefore $g > g_{bif}$. However, depending on the topology of the stable manifold, the trajectory of the suppressed cell can escape the stable fixed point and allow the cell to produce a spike for $g < g_{bif}$. This spike will inhibit the firing cell and allow the previously suppressed cell to start firing. Moreover, there exists a conductance value $g^\star$ and a condition $g > g^\star$ that is necessary for the suppressed cell to be release at all. In other words, only when $g > g^\star$ is satisfied can the network produce stable $n : n$ solutions, and produces the suppressed solution otherwise. The true value of the release conductance will depend on the type of $n : n$ solution and the coupling strength $\bar{g}$, and will lie in the interval $(g_{bif}, g^\star)$. As we will show in the following section, it turns out that $g^\star$ is a good approximation

trajectory to pass the fixed point and the cell to spike. We will derive the exact value of such a g_{min} in the following section, and to simplify the derivation our map assume that g_{min} is a good approximation for the release conductance, therefore setting $g^\star = g_{min}$. This assumption allows us to predict that timing of the release of the suppressed cell, that is precisely when

$$\bar{g}s = g^\star \tag{9}$$

215 is satisfied.

216   In summary: We assume that the release condition is sufficient to predict when the suppressed
217 cell is released. Due to the symmetry of $n : n$ solutions the release occurs at exactly half the period
218 of the full cycle, that is at $P/2$. The release time therefore uniquely determines the type of $n : n$
219 solution. Furthermore, computation of the release time does not depend on the membrane nor the
220 synaptic dynamics of the suppressed cell. Instead, the solution of the synaptic variable s of the free
221 cell is sufficient to predict when $g = g^*$ is satisfied. Finally, s is solely determined by the evolution
222 of the depression variable d of the free cell. Constructing a solution of d during the free phase
223 of either cell will therefore uniquely determine the solution of the full eight-dimensional network.
224 However, finding the solution d requires us to know the initial value $d(0)$ at the start of a cycle at
225 $t = 0$. In the next section we will construct a scalar return map that tracks these initial values $d(0)$
226 from cycle to cycle of stable $n : n$ solutions.

227 3.3   Construction of the scalar Poincaré map

228   In this section we construct the scalar Poincaré map $\Pi_n : d^\star \mapsto d^\star$. Here the discrete variable $d^\star$
229 tracks the values of the continuous depression variable d at the beginning of each $n : n$ burst. The
230 map Π_n therefore describes the evolution of d, of either of the two cells, from the beginning of one
231 cycle to the beginning of the next cycle. To simplify the map construction we will assume that a
232 free cell fires exactly n times before it becomes suppressed. We will construct Π_n by evolving d first
233 during the free phase and then during the suppressed phase of the $n : n$ limit cycle. First, let us
234 give explicit definitions of the free and suppressed phases. A schematic illustration of both phases
235 is given in fig. 7.

236   Suppose that at $t = 0$ cell 1 starts free with some initial $d(0)$. Cell 1 then fires n spikes at
237 the uncoupled period $T = T_{act} + T_{inact}$. Let $s(t)$ and $d(t)$ be the corresponding solutions of the
238 synaptic and depression variables of cell 1. After n spikes the total conductance $\bar{g}s(t)$ acting on
239 the suppressed cell 2 has decayed sufficiently to satisfy the release condition (9). That is at some
240 time $t = (n - 1)T + T_{act} + \Delta t$, where $\Delta t < T_{inact}$, we have $\bar{g}s(t) = g^\star$. Cell 2 is then released and
241 prevents cell 1 from further spiking. Here Δt is the time between the last spike of cell 1 and the
242 first spike of cell 2 [6]. Once released, cell 2 also fires n spikes until cell 1 becomes free once again.
243 Let P_n denote the full cycle period of a $n : n$ solution:

$$P_n = 2\Big((n - 1)T + T_{act} + \Delta t\Big). \tag{10}$$

244 We can now define the free and suppressed phases of cell 1 explicitly. The free phase is the interval
245 that lasts from the first spike time up until the beginning of the inactive phase of the last spike,
246 last spikes of the burst, that is for time $0 < t < (n - 1)T + T_{act}$. During the free phase of cell 1,
247 the suppressed cell 2 is inhibited sufficiently strong to prevent it from firing, hence $\bar{g}s > g^\star$. The
248 suppressed phase of cell 1 is the remaining duration of the cycle when the cell is not firing, that is
249 for $(n - 1)T + T_{act} < t < P_n$. Hence the suppressed phase lasts for $(n - 1)T + T_{act} + 2\Delta t$.

250   Note that only the suppressed phase depends on Δt, which will play a central role in the
251 construction of Π_n. From eq. (10) Δt can be computed as

$$\Delta t = \frac{1}{2}P_n - (n - 1)T - T_{act}. \tag{11}$$

252 We can use eq. (11) and the numerically computed bifurcation diagram of the period for stable $n : n$
253 solutions in fig. 4A to obtain the graph of Δt as a function of $\bar{g}$ (fig. 8). Each continuous branch of
254 Δt is monotonically increasing and corresponds to a $n : n$ burst: Stronger coupling $\bar{g}$ increases the
255 total synaptic conductance $\bar{g}s$ that acts on the suppressed cell, thus delaying its release. It is easy
256 to see that for any n-branch we have $\Delta t < T_{inact}$: Once Δt crosses T_{inact}, the free cell can "squeeze
257 in" an additional spike and the solutions bifurcate into a $(n + 1) - (n + 1)$ burst.

258   Distinguishing between the free and suppressed phases of a cycle allows us to describe the
259 dynamics of the depression variable d explicitly for each phase. As can be seen from fig. 7C,
260 during the free phase d depresses when $v > v_\theta$ and recovers when $v < v_\theta$. In contrast, during the

261 suppressed phase d only recovers and does not depress. Given the initial $d^\star = d(0)$ at the beginning
262 of the cycle and the number of spikes in the free phase n, we can now construct the burst map Π_n.
263 The map

$$\Pi_n(d^\star) = Q_n\big(F_n(d^\star)\big) \tag{12}$$

264 is a composition of two maps. Map

$$F_n : d^\star \mapsto \Delta t \tag{13}$$

265 models the evolution of d in the free phase. F_n takes an initial value $d^\star$ and calculates Δt. Map

$$Q_n : \Delta t \mapsto d^\star \tag{14}$$

266 models the recovery of d in the suppressed phase. Given some Δt map Q_n computes $d^\star$ at the start
267 of the next cycle.

268   Our aim in the following analysis is to elucidate the properties of Π_n and to understand the
269 structure of its parameter space by exploring how the stable and unstable fixed points of Π_n are
270 created. To that effect it will be useful to include not only positive, but also negative values of $d^\star$
271 to the domain of Π_n. But it is important to add that values $d^\star < 0$ are biologically impossible as
272 the depression variable models a finite pool of neurotransmitters, and therefore must be positive.
273 Because Π_n maps first from $d^\star$ to Δt, and then back to $d^\star$, we will also consider negative values of
274 Δt, interpreting them as $n : n$ solutions with partially overlapping bursts. As will become evident,
275 $\Delta t < 0$ is only a formal violation of the biological realism of the map Π_n, as numerically stable
276 $n : n$ solutions of the full system of ODEs only exist for $\Delta t > 0$.

277   We start the construction of Π_n by first considering the free phase and building the map F_n. At
278 each spike time t_k where $d(t_k) = d_k$, variable d decays first for the duration of the active phase of
279 the spike for T_{act}, as described by the solution to eq. (5). At $t = t_k + T_{act}$ we have

$$d(t_k + T_{act}) = d_k e^{-T_{act}/\tau_b}. \tag{15}$$

280 The depression variable then recovers during the inactive phase of the spike until t_{k+1}, where for
281 $0 < t < T_{inact}$:

$$d(t_{k+1}) = 1 - (1 - d_k e^{-T_{act}/\tau_b})e^{-t/\tau_a}. \tag{16}$$

282 By substituting $t = T_{inact}$ we can build a linear map that models the depression of d from spike
283 time t_k to the subsequent spike time t_{k+1} during the free phase:

$$d_{k+1} = \lambda\rho d_k + (1 - \rho), \tag{17}$$

where to keep the notation simple we let

$$\lambda := \exp(-T_{act}/\tau_b), \tag{18}$$

$$\rho := \exp(-T_{inact}/\tau_a). \tag{19}$$

284   Given constant T_{act} and T_{inact}, parameter λ determines how much the synapses depresses during
285 the active phase of the spike, while ρ determines how much it recovers during the inactive phase.
286 Since $0 < \lambda, \rho < 1$, the map in eq. (17) is increasing and contracting, with a fixed point at

$$d_s = \frac{1 - \rho}{1 - \lambda\rho}, \tag{20}$$

287 where $0 < d_s < 1$. The value d_s is the maximum depression value that can be observed in the
288 suppressed solution where the active cell fires at its uncoupled period T (see fig. 3E). Using the
289 release condition in eq. (9) allows us to derive the value of the minimum coupling strength that

290 will produce the full suppressed solution, denoted as $\bar{g}_s$. Solving eq. (7) for $s(t)$ with $t = T_{inact}$ and
291 setting the initial value $s(0) = d_s\lambda$ gives

$$\bar{g}_s d_s \lambda e^{-T_{inact}/\tau_\kappa} = g^\star. \tag{21}$$

292 By further substituting the definition of d_s in (20) and rearranging, we can write $\bar{g}_s$ as a function
293 of λ and ρ:

$$\bar{g}_s(\lambda, \rho) = \frac{1/\lambda - \rho}{1 - \rho} e^{T_{inact}/\tau_\kappa} g^\star. \tag{22}$$

294 Note that the above dependence of $\bar{g}_s$ on λ is linear and monotonically decreasing. Increasing λ
295 reduces the strength of the depression of the free cell. This in turn allows the free cell to fully
296 suppress the suppressed cell at smaller values of $\bar{g}$.

297 Solving eq. (17) gives us the linear map $\delta_n : d^\star \mapsto d_n$, that for some initial $d^\star$ computes the
298 depression at the nth spike time, $d_n = d(t_n)$:

$$\delta_n(d^\star) = (\lambda\rho)^{n-1}d^\star + (1 - \rho)\sum_{i=0}^{n-2}(\lambda\rho)^i. \tag{23}$$

299 Since $\lambda < 1$, function δ_n is a linearly increasing function of $d^\star$ with a fixed point at d_s for all n.
300 Having identified d after n spikes, we can now use the release condition $\bar{g}s = g^\star$ (eq. (9)) to find
301 Δt. At the last (nth) spike of the free phase at time $t_n = (n-1)T$ the synapse variable s is set to
302 the respective value of $d(t_n) = \delta_n(d^\star)$, and mirrors the value of d for the duration of T_{act}. at the
303 end of the active phase at time $t_n + T_{act}$ variable d has decayed to $\delta_n(d^\star)\lambda$ eq. (18), therefore

$$s(t_n + T_{act}) = \delta_n(d^\star)\lambda. \tag{24}$$

304 Finally s decays exponentially for $\Delta t < T_{inact}$. Solving ?? (case $v < v_\theta$) with initial condition
305 $s(0) = \delta_n(d^\star)\lambda$ yields:

$$s(\Delta t) = \delta_n(d^\star)\lambda e^{-\Delta t/\tau_\kappa}. \tag{25}$$

306 Substituting $s(\Delta t)$ into s of the release condition (eq. (9)) gives then

$$\bar{g}\delta_n(d^\star)\lambda e^{-\Delta t/\tau_\kappa} = g^\star. \tag{26}$$

307 Our assumption of the release condition guarantees that the suppressed cell 2 spikes and becomes
308 free when $\bar{g}s - g^\star$ crosses zero. Solving eq. (26) for Δt allows us to compute it a function of $d^\star$,
309 which defines our map F_n:

$$F_n(d^\star) := \tau_\kappa \ln\left(\frac{\bar{g}}{g^\star}\lambda\delta_n(d^\star)\right) = \Delta t. \tag{27}$$

310 Figure 9A shows F_n for various n, which is a strict monotonically increasing function of $d^\star$ as
311 well as $\bar{g}$. Larger values of $d^\star$ and $\bar{g}$, respectively, cause stronger inhibition of the suppressed cell,
312 and therefore prolong its release time and the associated Δt. Map F_n is defined on $d^\star > d_a$, where
313 d_a is a vertical asymptote found by solving $\delta_n(d^\star) = 0$ in eq. (23) for $d^\star$, which yields

$$d_a(n) = -\frac{(1-\rho)\sum_{i=0}^{n-2}(\lambda\rho)^i}{(\lambda\rho)^{n-1}} \leq 0 . \tag{28}$$

314 We now turn to the construction of map Q_n, which describes the recovery of the depression
315 variable during the suppressed phase. As we have identified earlier, the recovery in the suppressed

316 phase of a $n : n$ solution is of duration $(n-1)T + T_{act} + 2\Delta t$. Substituting that into the solution
317 of d (??) with the initial condition $d(0) = \delta_n(d^\star)\lambda$ yields the map Q_n:

$$Q_n(\Delta t) := 1 - (1 - \delta_n(d^\star)\lambda)e^{-((n-1)T+T_{act}+2\Delta t)/\tau_a}. \tag{29}$$

318 Given Δt, we can find $\delta_n(d^\star)$ by rearranging the release condition in eq. (26):

$$\delta_n(d^\star) = \frac{1}{\bar{g}\lambda}g^\star e^{\Delta t/\tau_\kappa}. \tag{30}$$

319 Map Q_n is shown in fig. 9B for various values n. Note that Q_n is monotonically increasing as larger
320 values Δt imply a longer recovery time, and hence Q_n grows without bound. All curves Q_n intersect
321 at some $\Delta t = \tau_\kappa \ln[\bar{g}/g^\star]$ where

$$Q_n\left[\tau_\kappa \ln\left(\frac{\bar{g}}{g^\star}\right)\right] = 1. \tag{31}$$

322 As we will show in the next section, all fixed points of the full map Π_n occur for $d^\star < 1$. We
323 will therefore restrict the domain of Q_n to $(-\infty, \tau_\kappa \ln[\bar{g}/(g^\star)])$ and the codomain to $(-\infty, 1)$.
324 Additionally, while values $\Delta t > T$ will be helpful in exploring the geometry of Π_n, recall from fig. 8
325 that in the flow system all $n : n$ solutions bifurcate into $(n+1) - (n+1)$ solutions exactly when
326 $\Delta t = T_{inact}$, and we will address this concern in the last part of our map analysis.

327   Having found F_n and Q_n, we can now construct the full map $\Pi_n(d^\star) = Q_n\big(F_n(d^\star)\big)$:

$$\Pi_n(d^\star) = 1 - \left(1 - \delta_n(d^\star)\lambda\right)\left(\frac{\bar{g}}{g^\star}\delta_n(d^\star)\lambda\right)^{-\tau}e^{-((n-1)T+T_{act})/\tau_a}, \tag{32}$$

328 where we substituted $\tau = 2\tau_k/\tau_a$. Since d is the slowest variable of the system and $\tau_a \gg \tau_\kappa$, we will
329 also assume $\tau < 1$. Figure 10A depicts Π_n for various n. Intersections of Π_n with the diagonal are
330 fixed points of the map. Figure 10B shows Π_2 with $n = 2$. Varying the synaptic strength $\bar{g}$ moves
331 the curves Π_n up and down the $(d^\star, \Pi_n)$-plane. For $\bar{g} < 0.03$ mS/cm^2 map Π_2 has no fixed points.
332 As $\bar{g}$ is increased to $\bar{g} \approx 0.03$ mS/cm^2, curve Π_2 coalesces with the diagonal tangentially. When
333 $\bar{g} > 0.03$ mS/cm^2, a pair of fixed points emerge, one stable and one unstable fixed point, indicating
334 the occurrence of a fold bifurcation of maps.

    From eq. (32) it is evident that Π_n is monotonically increasing with respect to $\bar{g}$ and also $d^\star$:

$$\frac{\mathrm{d}\Pi_n}{\mathrm{d}\bar{g}} > 0, \tag{33}$$

$$\frac{\mathrm{d}\Pi_n}{\mathrm{d}d^\star} > 0, \tag{34}$$

335 and in the following sections we will heavily rely on this monotonicity property of Π_n. Just as F_n,
336 curves Π_n spawn at the asymptote d_a (eq. (28)), and because

$$\lim_{\bar{g}\to\infty} \Pi_n = 1 \text{ for all } n, \tag{35}$$

337 fixed points of Π_n lie in $(d_a, 1)$.

338 ## 3.4   Existence and stability of fixed points

339   We introduce the fixed point notation $d_f^\star$ with $\Pi_n(d_f^\star) = d_f^\star$. The existence of fixed points $d_f^\star$
340 for $\bar{g}$ sufficiently large can be shown from the strict monotonicity of Π_n with respect to $\bar{g}$ and $d^\star$
341 (eqs. (33) and (34)), as well as the fact that the slope of Π_n is monotonically decreasing,

$$\left(\frac{\mathrm{d}}{\mathrm{d}d^\star}\right)^2 \Pi_n < 0. \tag{36}$$

In the limit $d^\star \to d_a$ the value of Π_n decreases without bound for any $\bar{g} > 0$. In the limit $\bar{g} \to 0$, Π_n
also decreases without bound, but as $\bar{g} \to \infty$ values of Π_n approach 1. It follows from eq. (33) and

the intermediate value theorem that for some $\bar{g}$ large enough Π_n intersects the diagonal. Moreover, because Π_n and its slope are monotonic with respect to $d^\star$, there exists some critical fixed point $(d_b^\star, \bar{g}_b)$ where Π_n aligns with the diagonal tangentially with

$$\Pi_n(d_b^\star, \bar{g}_b) = d_b^\star, \tag{37}$$

$$\frac{d}{d^\star}\Pi_n(d_b^\star, \bar{g}_b) = 1. \tag{38}$$

Equations (33) and (36) constitute the non-degeneracy conditions for a codimension-1 fold bifurcation of maps, indicating that in a neighbourhood of $(d_b^\star, \bar{g}_b)$ map Π_n has the topological normal form described by the graph of

$$x \mapsto \beta + x - x^2, \tag{39}$$

with a stable and unstable fixed point $x = \pm\sqrt{\beta}$, and slopes $dx/d\beta = \mp(2\sqrt{\beta})^{-1}$, respectively.

3.5 Fold bifurcations of maps

Fixed points of Π_n satisfy the fixed point equation

$$\Phi_n(d^\star, \bar{g}) := \Pi_n(d^\star, \bar{g}) - d^\star = 0. \tag{40}$$

As we have already shown, for $\bar{g} > \bar{g}_b(n)$ solutions to eq. (40) exist in pairs of stable and unstable fixed points. Solving eq. (40) explicitly for $d^\star$ it not trivial, but solving for $\bar{g}$ is straightforward and given by $\bar{g} = G_n(d^\star)$, where

$$G_n(d^\star) := \frac{g^\star}{\delta_n(d^\star)\lambda}\left(\frac{(1 - \lambda\delta_n(d^\star))}{1 - d^\star}e^{-((n-1)T + T_{act})/\tau_a}\right)^{1/\tau} \tag{41}$$

is defined for $d^\star < 1$ and $\delta_n(d^\star) > 0$. Plotting $d^\star$ against $\bar{g}$ gives the fixed point curves, which are shown in fig. 11A. Note the typical quadratic shape of a fold bifurcation of maps. It is also evident that the fold bifurcations occur for increasingly smaller $\bar{g}$ as n is increased. Moreover, we can observe that unstable fixed points have negative values of $d^\star$ for $n > 1$.

Equation (41) also allows us to find the critical fixed point connected with the fold bifurcation, namely $(d_b^\star(n), \bar{g}_b(n))$, which is the global minimum of $G_n(d_f^\star)$:

$$d_b^\star(n) = \operatorname{argmin} G_n(d_f^\star), \tag{42}$$

$$\bar{g}_b(n) = \min G_n(d_f^\star). \tag{43}$$

Function G_n is strictly monotonic on the respective intervals of $d_f^\star$ that correspond to the stable and unstable fixed points, that is

$$\frac{dG_n}{dd_f^\star} < 0, \text{ for } d_f^\star > d_b^\star(n) \text{ stable}, \tag{44}$$

$$\frac{dG_n}{dd_f^\star} > 0, \text{ for } d_f^\star < d_b^\star(n) \text{ unstable}, \tag{45}$$

which allows us to express the stable and unstable fixed points as the inverse of G_n on their respective intervals of $d_f^\star$. Because we are primarily interested in the stable fixed points, we define the stable fixed point function $d_f^\star = \phi_n(\bar{g})$ as

$$\phi_n(\bar{g}) := G_n^{-1}(d_f^\star) \text{ for } d_f^\star > d_b^\star(n). \tag{46}$$

Function $\phi_n(\bar{g})$ is also monotonic, and is therefore straightforward to compute numerically. Here we use the Python package Pynverse [20] for that purpose.

Having found the stable fixed points $d_f^\star$ as a function of $\bar{g}$, we can now compute the associated cycle period. Recall that the period is given by eq. (10), which we can be written as a function of $\bar{g}$:

$$P_n(\bar{g}) = 2\Big((n-1)T + T_{act} + F_n\big(\underbrace{\phi_n(\bar{g}),\bar{g}}_{d_f^\star}\big)\Big), \tag{47}$$

where map F_n (eq. (27)) calculates Δt given a stable fixed point $d_f^\star = \phi_n(\bar{g})$. We plot the predicted period $P_n(\bar{g})$ versus the cycle period that was computed from numerically integrating the full system of ODEs in fig. 11B. For $n > 1$ our map Π_n accurately predicts the period. When laying out our assumptions in section 3.2, we have already predicted an inaccuracy for $n = 1$ (see fig. 6), since here $\bar{g}$ is not sufficiently strong to guarantee the validity of our release condition (eq. (9)).

It is evident from fig. 11A that ϕ_n is strictly increasing with $\bar{g}$. This property follows directly from the normal form of the fold bifurcation (eq. (39)), but can also be shown using implicit differentiation and the fixed point equation $\Phi_n(\phi_n(\bar{g}),\bar{g}) = 0$ in eq. (40). For $d_f^\star = \phi_n(\bar{g}) > d_b(n)$ we get:

$$\frac{d\phi_n}{d\bar{g}} = -\frac{\partial\Phi_n/\partial\bar{g}}{\partial\Phi_n/\partial d^\star} = \frac{\partial\Pi_n/\partial\bar{g}}{1 - \partial\Pi_n/\partial d^\star} > 0. \tag{48}$$

The inequality follows from $\partial\Pi_n/\partial\bar{g} > 0$ and the fact that $\partial\Pi_n/\partial d^\star < 1$ for $d^\star > d_b(n)$. ?? allows us to explain why the period P_n increases with $\bar{g}$, as seen in fig. 11B. Differentiating P_n gives:

$$\frac{dP_n}{d\bar{g}} = 2\boldsymbol{\nabla}F_n(d_f^\star,\bar{g}) \cdot \begin{bmatrix} \partial\phi_n/\partial\bar{g} \\ 1 \end{bmatrix} > 0, \tag{49}$$

where the partial derivatives of $F_n(d_f^\star,\bar{g})$ are:

$$\frac{\partial F_n}{\partial d_f^\star} = \tau_s \frac{(\lambda\rho)^{n-1}}{\delta_n(d_f^\star)} > 0, \tag{50}$$

$$\frac{\partial F_n}{\partial\bar{g}} = \frac{\tau_s}{\bar{g}} > 0. \tag{51}$$

?? and eq. (49) have an intuitive biological interpretation: Increasing the coupling strength between the neurons leads to overall stronger inhibition of the suppressed cell, which delays its release and leads to a longer cycle period. The latter allows more time for the synapse to depress in the free phase and recover in the suppressed phase, resulting in overall larger values of $d_f^\star$, that is weaker depression at the burst onset.

While fixed points of our Poincaré map predict the cycle period of the flow system excellently, its construction relies on the strong assumption that the free phase contains exactly n spikes. As is evident from fig. 11B this assumption is clearly violated in the flow system, as stable $n : n$ bursts exists only on certain parameter intervals of $\bar{g}$. In the last sub-section we will analyse the mechanisms that guide how the stable $n : n$ are created and destroyed, and use our previous analysis to derive the corresponding parameter intervals of $\bar{g}$ where such solutions exist.

3.6   Period increment bifurcations with co-existent attractors

Let $\bar{g}_+(n)$ and $\bar{g}_-(n)$ denote the left and right parameter borders on $\bar{g}$ where stable $n : n$ solutions exist. That is, as $\bar{g}$ is increased stable $n : n$ solutions are created at $\bar{g}_+(n)$ and destroyed at $\bar{g}_-(n)$. When $\bar{g}$ is reduced beyond $\bar{g}_+(n)$, $n : n$ solutions bifurcate into $(n-1)-(n-1)$ solutions, while when $\bar{g}$ is increased beyond $\bar{g}_-(n)$, $n : n$ solutions bifurcate into $(n+1)-(n+1)$ solutions. Let us briefly recap our observations regarding $\bar{g}_+(n)$ and $\bar{g}_-(n)$ from the numerical bifurcation diagram

in fig. 11B. For $n > 1$ there are the following relations:

$$\bar{g}_+(n) < \bar{g}_-(n), \tag{52}$$

$$\bar{g}_+(n) < \bar{g}_+(n+1) \text{ and } \bar{g}_-(n) < \bar{g}_-(n+1), \tag{53}$$

$$\bar{g}_+(n+1) < \bar{g}_-(n), \tag{54}$$

$$\bar{g}_-(n+1) - \bar{g}_+(n+1) < \bar{g}_-(n) - \bar{g}_-(n). \tag{55}$$

Equations (52) and (53) are self-explanatory. Equation (54) formally describes occurrence of co-existence between stable $n : n$ and $(n + 1) - (n + 1)$ solutions. Equation (55) implies that the parameter interval on $\bar{g}$ of $n : n$ solutions decreases with n, in other words, bursts with more spikes occur on increasingly smaller intervals of the coupling strength. All of the above relations are reminiscent of the period increment bifurcations with co-existent attractors, first described for piecewise-linear scalar maps with a single discontinuity by Avrutin and colleagues [e.g. see 21, 22, 23, 21]. While our maps Π_n are fully continuous, the above observation suggests that a different piecewise-linear scalar map that captures the period increment bifurcations of the full system might exist. We will explore what such a map might look like in the discussion.

Let us now find algebraic equations that will allow us to calculate the critical parameters $\bar{g}_+(n)$ and $\bar{g}_-(n)$ associated with the period increment bifurcations. Recall that the period P_n derived from the fixed points of Π_n is an increasing function of $\bar{g}$:

$$\frac{\mathrm{d}P_n}{\mathrm{d}\bar{g}} = 2\frac{\mathrm{d}F_n(\phi_n(\bar{g}), \bar{g})}{\mathrm{d}\bar{g}} > 0, \tag{56}$$

that is, as the coupling strength increases, it takes longer for the total synaptic conductance to fall below the value of the release conductance, which delays the release of the suppressed cell, and Δt becomes larger. When $\Delta t > T_{inact}$, the free cell can produce another spike and the solution bifurcates into a $(n + 1) - (n + 1)$ solution. Note, however, that at $\bar{g}_+(n)$ the bifurcation into a $(n - 1) - (n - 1)$ does not occur at $\Delta t = 0$. Here the mechanism is different: A sufficient reduction of $\bar{g}$ causes the total synaptic conductance to drop below the release conductance in the previous ISI, which allows the suppressed cell to be released one spike earlier.

Using the above reasoning we can now formulate the conditions for both bifurcations at $\bar{g}_+(n)$ and $\bar{g}_-(n)$. As in the previous sections, we will only restrict ourselves to the analysis of the stable fixed points given implicitly by $d_f^\star = \phi_n(\bar{g})$ (eq. (46)). At the right bifurcation border $\bar{g}_-(n)$ we have $\Delta t = T_{inact}$, and after substituting our F_n map (eq. (27)) this translates into

$$F_n(\phi_n(\bar{g}), \bar{g}) = T_{inact}, \tag{57}$$

which lets us define a function

$$\mathcal{R}_n(\bar{g}) := F_n(\phi_n(\bar{g}), \bar{g}) - T_{inact}, \tag{58}$$

whose root is the desired right bifurcation border $\bar{g}_-(n)$. In case of the left bifurcation border at $\bar{g}_+(n)$, the release condition is satisfied just before the free cell has produced its nth spike, where total synaptic conductance is given by

$$\bar{g}\delta_{n-1}\big(\phi_n(\bar{g})\big)\lambda e^{-T_{inact}/\tau_\kappa} = g^\star, \tag{59}$$

which can be rewritten as a function

$$\mathcal{L}_n(\bar{g}) := \bar{g}\delta_{n-1}\big(\phi_n(\bar{g})\big)\lambda e^{-T_{inact}/\tau_\kappa} - g^\star, \tag{60}$$

whose root is $\bar{g}_+(n)$. Both $\mathcal{R}_n$ and $\mathcal{L}_n$ are increasing with respect to $\bar{g}$, which makes finding their roots numerically straightforward.

Figure 12 shows the period $P_n(\bar{g})$ as predicted by the fixed points of Π_n (eq. (47)) plotted on their respective intervals $\bar{g} \in [\bar{g}_+(n), \bar{g}_-(n)]$ (blue), as well as the cycle period acquired from numerical

418 integration of the full system of ODEs (orange). Note that the width of $n : n$ branches decreases with
419 n, which confirms the inequality in eq. (55). That is, bursts with more spikes occur on increasingly
420 smaller intervals of $\bar{g}$, which can be interpreted as a lost of robustness with respect to the coupling
421 strength of long-cyclic solutions. We also note the occurrence of bi-stability between pairs of $n : n$
422 and $(n + 1) - (n + 1)$ branches, which also confirms our initial observation in eq. (54).

423 As previously observed in fig. 11B our maps prediction of the cycle period is accurate for $n > 1$.
424 Recall that our reduction assumptions required a sufficiently large coupling strength, which we
425 numerically estimated to be $\bar{g} \approx 0.592 \mathrm{mS/cm^2}$ in fig. 6. The mismatch in period for $1 - 1$ solutions,
426 but also the mismatch in the left bifurcation border $\bar{g}_-(n = 2)$ of the $2 - 2$ solution can be attributed
427 to the violation of that assumption. However, even for branches of large $n : n$ solutions there is
428 a mismatch between the bifurcation borders. Presumably our assumptions on the time scales of
429 w and s dynamics do not hold here, and can only be captured by more complex approximations.
430 Nevertheless, our map allows approximate extrapolation of the cycle period and the respective
431 bifurcation borders where numerical integration of the ODEs would require a very small time step.

4 DISCUSSION

432 Synaptic depression of inhibition is believed to play an important role in the generation of rhythmic
433 activity involved in many motor rhythms such as in leech swimming [24] and leech heart beat [25],
434 and in the lobster pyloric system [1, 2]. In inhibitory half-centre CPGs, such as believed to be
435 found in the struggling network of Xenopus tapdoles, synaptic depression can act as a burst
436 termination mechanism, enabling the alternation of bursting between the two sides of the CPG [11].
437 Mathematical modelling can shed light on the underlying mechanisms that enable the generation
438 of such anti-phase bursts, and help identify the components that control this rhythm allowing it to
439 switch between different patterns.

440 To study the mechanisms of burst generation in half-centre CPGs we have analysed a neuronal
441 model network that consists of a pair of inhibitory neurons that undergo a frequency dependent
442 synaptic depression. When the strength of synaptic inhibition between the neurons is varied, such
443 a simple network can display a range of different $n : n$ burst patterns. Using the timescale disparity
444 between neuronal and synaptic dynamics, we have reduced the network model of eight ODEs to a
445 scalar first return map Π_n of the slow depression variable d. This map Π_n is a composition of two
446 maps, F_n and Q_n, that model the evolution of the depression during the free and quiet phases of
447 $n : n$ solutions respectively. Both F_n and Q_n maps are constructed by using the dynamics of single
448 uncoupled neurons. Fixed points of Π_n are created in pairs through a fold bifurcation of maps,
449 where the stable fixed point correspond to stable $n : n$ burst solutions of the full two-cell system
450 of ODEs. The results from our one-dimensional map match excellently with numerical simulation
451 of the full network. Our results are in line with Brown's 1911 rhythmogenesis hypothesis, namely
452 that synaptic depression of inhibition is a mechanism by which anti-phase bursting may arise.

453 We have studied $n : n$ solutions assuming that the synaptic coupling $\bar{g}$ between the two cells
454 is symmetrical. However, Bose and Booth [6] have shown that asymmetrical coupling $(\bar{g}_1, \bar{g}_2)$ can
455 result in network solutions of type $m - n$, where one cell fires m spikes, while the other n spikes.
456 It is conceivable that our map construction can be extended to also capture such $m - n$ solutions.
457 Remember, in the case of symmetrical coupling with $n : n$ solutions, the timecourse of the depression
458 variables d_1 and d_2 were in anti-phase, and it was therefore sufficient to track only one of the two
459 variables. To capture the full network dynamics in case of asymmetrical coupling one would also
460 have to account for burst patterns of type $m - n$, where the solutions of the depression variables
461 d_1 and d_2 are not simply time-shifted versions of each other. To do that, one could track the state
462 of both variables by constructing a two-dimensional Poincaré map $\Pi(d_1, d_2)$. While geometrical
463 interpretation of two-dimensional maps remains challenging, there exist a number of recent studies
464 which have employed novel geometrical analysis methods to understand the dynamics of two-
465 dimensional maps of small neuronal networks [26, 27, 28]. Generally speaking, our map construction
466 approach is applicable to any small network, even with more than two neurons. As long as the
467 network dynamics occur on separable timescales the main challenges to the map construction lie
468 in identifying the slowest variables, and finding an appropriate, simplified description of their

respective timecourses. In theory, the reduction approach can be also applied to neuronal systems with more than two timescales [e.g. see 29].

In tadpoles, struggling is believed to be initiated by an increase in the firing frequency of reciprocally inhibitory commisural interneurons, which has been hypothesised to lead to stronger synaptic depression of inhibition and result in the iconic anti-phase bursting [11]. It would therefore be interesting to study how varying the cell intrinsic firing period T could affect the network rhythm. While we have laid out the framework to perform such an investigation, due to the choice of neural model we have avoided varying T. Recall that T is a derived parameter in the Morris and Lecar [12] model, and can therefore not be varied in isolation of other model parameters. This makes verifying any analytical results from our map analysis via numerical integration of the ODEs difficult. A more abstract model such as the quadratic integrate-and-fire model [30] allows varying T independently of other model parameters, and could be more fitting in this scenario.

Our simulations of the network showed that $n : n$ solutions lose robustness as their period is increased. That is, solutions with a larger cycle period occur on increasingly smaller intervals of the coupling strength. We were able to replicate this finding by numerically finding the respective left and right borders of stable $n : n$ branches of fixed points of Π_n, and showing that the distance between these borders shrinks with n. We have also noted the resemblance of our bifurcation diagram to one where such $n : n$ branches are created via a period-increment bifurcation with co-existent attractors of scalar linear maps with a discontinuity [31, 23]. It is worthwhile noting that the bifurcations of piecewise linear maps studied by Avrutin et al. and colleagues result from a "reinjection" mechanism, first described by Perez [32]. Here the orbit of a map performs multiple iterations on one side of the discontinuity, before jumping to the other side and being reinjected back into the initial side of the discontinuity. The stark difference of such a map to our map is that reinjection allows a single scalar map to produce periodic solutions of varying periods. In contrast, we rely on n different maps Π_n to describe the burst dynamics without explicitly capturing the period increment bifurcations. It is therefore conceivable that despite the complexity and non-linearity of the dynamics of our two-cell network, a single piecewise-linear map might be already sufficient to capture the mechanisms that shape the parameter space of the full system. In their discussion, Bose and Booth [6] briefly outline ideas about how such a linear map could be constructed.

In addition to stable $n : n$ solutions, the numerical continuation by Bose and Booth [6] also revealed branches of unstable $n : n$ solutions. While we have identified fold bifurcations of our burst map, we have not found corresponding bifurcations of the flow ODE system, and have generally ignored the significance of unstable map fixed points. However, the quadratic nature of the period bifurcation curve is reminiscent of a saddle-node on an invariance circle (SNIC) bifurcation, where the oscillation period lengthens and finally becomes infinite as a limit cycle coalesces with a saddle point. SNIC bifurcations have been studied in great detail [e.g. 33], and a next step would be to provide a rigorous explanation of not only the map dynamics, but also of the flow dynamics of the ODE system.

We have shown that when the strength of the maximum synaptic conductance is varied, synaptic depression of inhibition can enable our two-cell network to produce burst solutions of different periods. This result is in line with the idea that one role of synaptic depression in the nervous system may be to allow a finite size neuronal network to participate in different tasks by producing a large number of rhythms [6, 34, 11]. To change from one rhythm to another would only require a reconfiguration of the network through changes in synaptic coupling strength, which can occur through the process of learning. Thus short-term synaptic depression of inhibition may provide means for a network to adapt to environmental challenges without changing its topology, that is without the introduction or removal of neurons.

CONFLICT OF INTEREST STATEMENT

The authors declare that the research was conducted in the absence of any commercial or financial relationships that could be construed as a potential conflict of interest.

AUTHOR CONTRIBUTIONS

MO and CH contributed to conception and design of the study. MO performed numerical computation and analysis. All authors contributed to manuscript writing and revision.

FUNDING

ACKNOWLEDGEMENTS

DATA AVAILABILITY STATEMENT

The datasets generated for this study are available on request to the corresponding author.

REFERENCES

[1] Manor Y, Nadim F, Abbott L, Marder E. Temporal dynamics of graded synaptic transmission in the lobster stomatogastric ganglion. Journal of Neuroscience 17 (1997) 5610–5621. doi:10.1523/JNEUROSCI.17-14-05610.1997.

[2] Rabbah P, Nadim F. Distinct synaptic dynamics of heterogeneous pacemaker neurons in an oscillatory network. Journal of neurophysiology 97 (2007) 2239–2253. doi:10.1152/jn.01161.2006.

[3] Donovan M, Wenner P, Chub N, Tabak J, Rinzel J. Mechanisms of spontaneous activity in the developing spinal cord and their relevance to locomotion. Annals of the New York Academy of Sciences 860 (1998) 130–141.

[4] Nadim F, Manor Y. The role of short-term synaptic dynamics in motor control. Current Opinion in Neurobiology 10 (2000) 683–690. doi:10.1016/S0959-4388(00)00159-8.

[5] Nadim F, Manor Y, Kopell N, Marder E. Synaptic depression creates a switch that controls the frequency of an oscillatory circuit. Proceedings of the National Academy of Sciences 96 (1999) 8206–8211. doi:10.1073/pnas.96.14.8206.

[6] Bose A, Booth V. Co-existent activity patterns in inhibitory neuronal networks with short-term synaptic depression. Journal of Theoretical Biology 272 (2011) 42–54. doi:10.1016/j.jtbi.2010.12.001.

[7] Brown TG. The intrinsic factors in the act of progression in the mammal. Proceedings of the Royal Society of London. Series B 84 (1911) 308–319.

[8] Reiss RF. A theory and simulation of rhythmic behavior due to reciprocal inhibition in small nerve nets. Proceedings of the May 1-3, 1962, spring joint computer conference (ACM) (1962), 171–194. doi:10.1145/1460833.1460854.

[9] Perkel DH, Mulloney B. Motor pattern production in reciprocally inhibitory neurons exhibiting postinhibitory rebound. Science 185 (1974) 181–183. doi:10.1126/science.185.4146.181.

[10] Friesen WO. Reciprocal inhibition: a mechanism underlying oscillatory animal movements. Neuroscience & Biobehavioral Reviews 18 (1994) 547–553. doi:10.1016/0149-7634(94)90010-8.

[11] Li WC, Sautois B, Roberts A, Soffe SR. Reconfiguration of a vertebrate motor network: specific neuron recruitment and context-dependent synaptic plasticity. The Journal of Neuroscience 27 (2007) 12267–12276. doi:10.1523/JNEUROSCI.3694-07.2007.

[12] Morris C, Lecar H. Voltage oscillations in the barnacle giant muscle fiber. Biophysical Journal 35 (1981) 193–213. doi:10.1016/S0006-3495(81)84782-0.

[13] Matveev V, Bose A, Nadim F. Capturing the bursting dynamics of a two-cell inhibitory network using a one-dimensional map. Journal of Computational Neuroscience 23 (2007) 169–187. doi:10.1007/s10827-007-0026-x.

[14] Bose A, Manor Y, Nadim F. Bistable oscillations arising from synaptic depression. SIAM Journal on Applied Mathematics 62 (2001) 706–727. doi:10.1137/S0036139900378050.

[15] Tsodyks MV, Markram H. The neural code between neocortical pyramidal neurons depends on neurotransmitter release probability. Proceedings of the National Academy of Sciences 94 (1997) 719–723. doi:10.1073/pnas.94.2.719.

[16] Ermentrout GB, Terman DH. Mathematical foundations of neuroscience, Interdisciplinary Applied Mathematics, vol. 35 (Springer New York) (2010). doi:10.1007/978-0-387-87708-2.

[17] Ermentrout B. Simulating, analyzing, and animating dynamical systems: a guide to xppaut for researchers and students (SIAM) (2002).

[18] Virtanen P, Gommers R, Oliphant TE, Haberland M, Reddy T, Cournapeau D, et al. SciPy 1.0: Fundamental Algorithms for Scientific Computing in Python. Nature Methods 17 (2020) 261–272. doi:10.1038/s41592-019-0686-2.

[19] [Dataset] Olenik M. PyXPP. https://github.com/markolenik/PyXPP (2021).

[20] [Dataset] Gonzalez AS. pynverse. https://github.com/alvarosg/pynverse (2021).

[21] Gardini L, Avrutin V, Schanz M, Granados A, Sushko I. Organizing centers in parameter space of discontinuous 1d maps. the case of increasing/decreasing branches. ESAIM: Proceedings 36 (2012) 106–120. doi:10.1051/proc/201236009.

[22] Tramontana F, Gardini L, Avrutin V, Schanz M. Period adding in piecewise linear maps with two discontinuities. International Journal of Bifurcation and Chaos 22 (2012) 1250068. doi:10.1142/s021812741250068x.

[23] Avrutin V, Granados A, Schanz M. Sufficient conditions for a period incrementing big bang bifurcation in one-dimensional maps. Nonlinearity 24 (2011) 2575–2598. doi:10.1088/0951-7715/24/9/012.

[24] Mangan P, Cometa A, Friesen W. Modulation of swimming behavior in the medicinal leech. IV. Serotonin-induced alteration of synaptic interactions between neurons of the swim circuit. Journal of comparative physiology. A, Sensory, neural, and behavioral physiology 175 (1994) 723–736. doi:10.1007/BF00191844.

[25] Calabrese RL, Nadim F, Olsen ØH. Heartbeat control in the medicinal leech: A model system for understanding the origin, coordination, and modulation of rhythmic motor patterns. Journal of neurobiology 27 (1995) 390–402. doi:10.1002/neu.480270311.

[26] Akcay Z, Bose A, Nadim F. Effects of synaptic plasticity on phase and period locking in a network of two oscillatory neurons. The Journal of Mathematical Neuroscience 4 (2014) 8. doi:10.1186/2190-8567-4-8.

[27] Akcay Z, Huang X, Nadim F, Bose A. Phase-locking and bistability in neuronal networks with synaptic depression. Physica D: Nonlinear Phenomena 364 (2018) 8 – 21. doi:10.1016/j.physd.2017.09.007.

[28] Liao G, Diekman C, Bose A. Entrainment Dynamics of Forced Hierarchical Circadian Systems Revealed by 2-Dimensional Maps. SIAM J. Appl. Dyn. Syst. (2020).

[29] Kuehn C. Multiple Time Scale Dynamics, Applied Mathematical Sciences, vol. 191 (Springer International Publishing) (2015). doi:10.1007/978-3-319-12316-5.

[30] Izhikevich EM. Which model to use for cortical spiking neurons? IEEE transactions on neural networks 15 (2004) 1063–1070. doi:10.1109/TNN.2004.832719.

[31] Avrutin V, Schanz M, Schenke B. Breaking the continuity of a piecewise linear map. ESAIM: Proceedings 36 (2012) 73–105. doi:10.1051/proc/201236008.

[32] Perez JM. Mechanism for global features of chaos in a driven nonlinear oscillator. Physical Review A 32 (1985) 2513–2516. doi:10.1103/physreva.32.2513.

[33] Ermentrout G, Kopell N. Parabolic bursting in an excitable System coupled with a slow oscillation. SIAM Journal on Applied Mathematics 46 (1986) 233–253. doi:10.1137/0146017.

[34] Jalil S, Grigull J, Skinner FK. Novel bursting patterns emerging from model inhibitory networks with synaptic depression. Journal of Computational Neuroscience 17 (2004) 31–45. doi:10.1023/B:JCNS.0000023870.23322.0a.
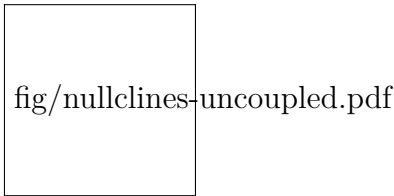
FIGURE CAPTIONS

fig/nullclines-uncoupled.pdf

Figure 1. Periodic solution of relaxation-oscillator model neuron. **(A)** Projection of limit cycle onto (v, w)-phase plane with v-nullcline (blue, v_∞) and w-nullcline (orange, w_∞). Unstable fixed point p_f is indicated by an orange dot. **(B)** Corresponding voltage trace $v(t)$ of an action potential.
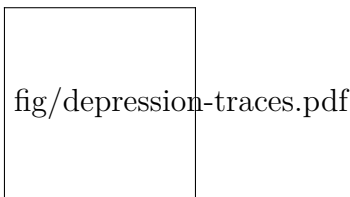
fig/depression-traces.pdf

Figure 2. Solution profiles of a $4 - 4$ burst. **(A)** Membrane potentials of cell 1 (v_1, blue), and cell 2 (v_2, orange). **(B)** Synaptic variables d_1 (blue) and s_1 (grey) of cell 1.

fig/burst-sols.pdf
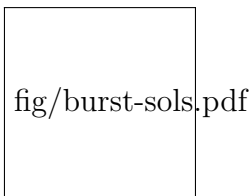
Figure 3. Voltage traces of both cells of numerically stable solutions for increasing values of the coupling strength $\bar{g}$ (increasing top to bottom).

fig/bif-diagram.pdf
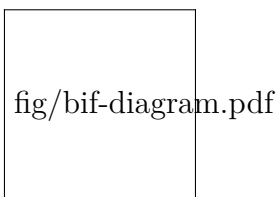
Figure 4. Numerically computed bifurcation diagrams of stable $n : n$ solutions for increasing coupling strength $\bar{g}$. **(A)** Period of stable solutions. Dashed lines show the interval between the $5 - 5$ and the suppressed solutions, where higher period $n : n$ solutions occur on increasingly smaller intervals of $\bar{g}$. **(B)** ISIs corresponding to $n : n$ solutions in (A). Long ISIs are associated with the quiet phase of a burst, short ISIs with the free phase. During the free phase, ISIs are of approximately constant duration T.

Figure 5. Nullclines v_∞ (blue) and w_∞ (orange) in the (v, w)-phase plane for different values of the total synaptic conductance $\bar{g}s$. For small $\bar{g}s < g^\star$, fixed point p_f is unstable (orange point). Larger values $\bar{g}s$ move v_∞ down in the (v, w)-plane until p_f changes stability (half orange, half blue point) at some critical total conductance value $\bar{g}s = g^\star$, and becomes stable (blue point) for $\bar{g} > g^\star$.
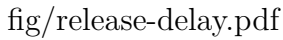

Figure 6. Numerically computed values of the release delay for varying $\bar{g}$. Each of the three branches (A, B, C) also shows the timecourse of the total synaptic conductance $\bar{g}s$ of a sample stable solution of both cells (blue and orange), as well as the release conductance $g^\star$ (dashed green line). **(A)** Branch corresponding to the $1 - 1$ solution. Here the quiet cell only spikes after a significant release delay. **(B)** Branch with a long release delay associated with a subset of $2 - 2$ solutions. Here the release condition is briefly satisfied after the first spike of cell 1. This does not cause firing of cell 2, which only occurs after the second spike of cell 1. **(C)** Branch with $n : n$ solutions where release delay is approximately zero and the release condition is sufficient for firing of cell 2.
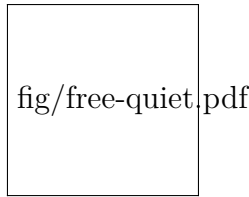
Figure 7. Schematic diagram of the free and quiet phases for a $3-3$ solution. **(A)** Membrane potentials of cell 1 (v_1) and cell 2 (v_2). The grey patches depict inter-burst-intervals Δt. **(B)** Total synaptic conductance of cell 1 ($\bar{g}s_1$) as it crosses the release conductance $g^\star$. **(C)** Solution $d_1(t)$ of depression variable of cell 1, during free (blue) and quiet phases (orange).
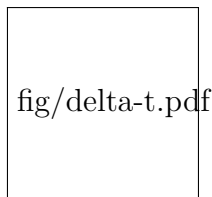

Figure 8. Numerically computed bifurcation diagram of Δt for varying $\bar{g}$. Each continuous branch is associated with a stable $n : n$ burst solution. Increasing $\bar{g}$ increases Δt until the solutions bifurcate at $\Delta t \approx T$.
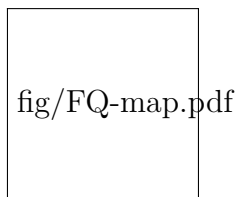

Figure 9. Maps F_n **(A)** and Q_n **(B)** for $\bar{g} = 0.6$ mS/cm^2 and $n = 1, 2, 3, 4$. Curves F_n intersect at d_s which is indicated by a dashed vertical line.
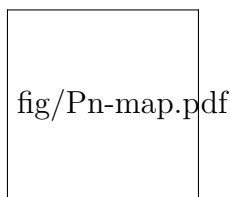

Figure 10. Map $\Pi_n : d^\star$. **(A)** Π_n for $n = 1, 2, 3, 4$ at $\bar{g} = 0.6$ mS/cm^2. **(B)** Π_2 with $n = 2$ for varying $\bar{g} \approx 0.01, 0.034, 0.3$ mS/cm^2. The identity function is illustrated by a diagonal line.
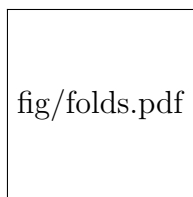

Figure 11. **(A)** Fold bifurcation diagrams of stable (continuous curves) and unstable (dotted curves) fixed points of Π_n for varying n. **(B)** Cycle periods computed from stable fixed points (blue), and the corresponding solution period from numerical integration of the system of ODEs (orange).
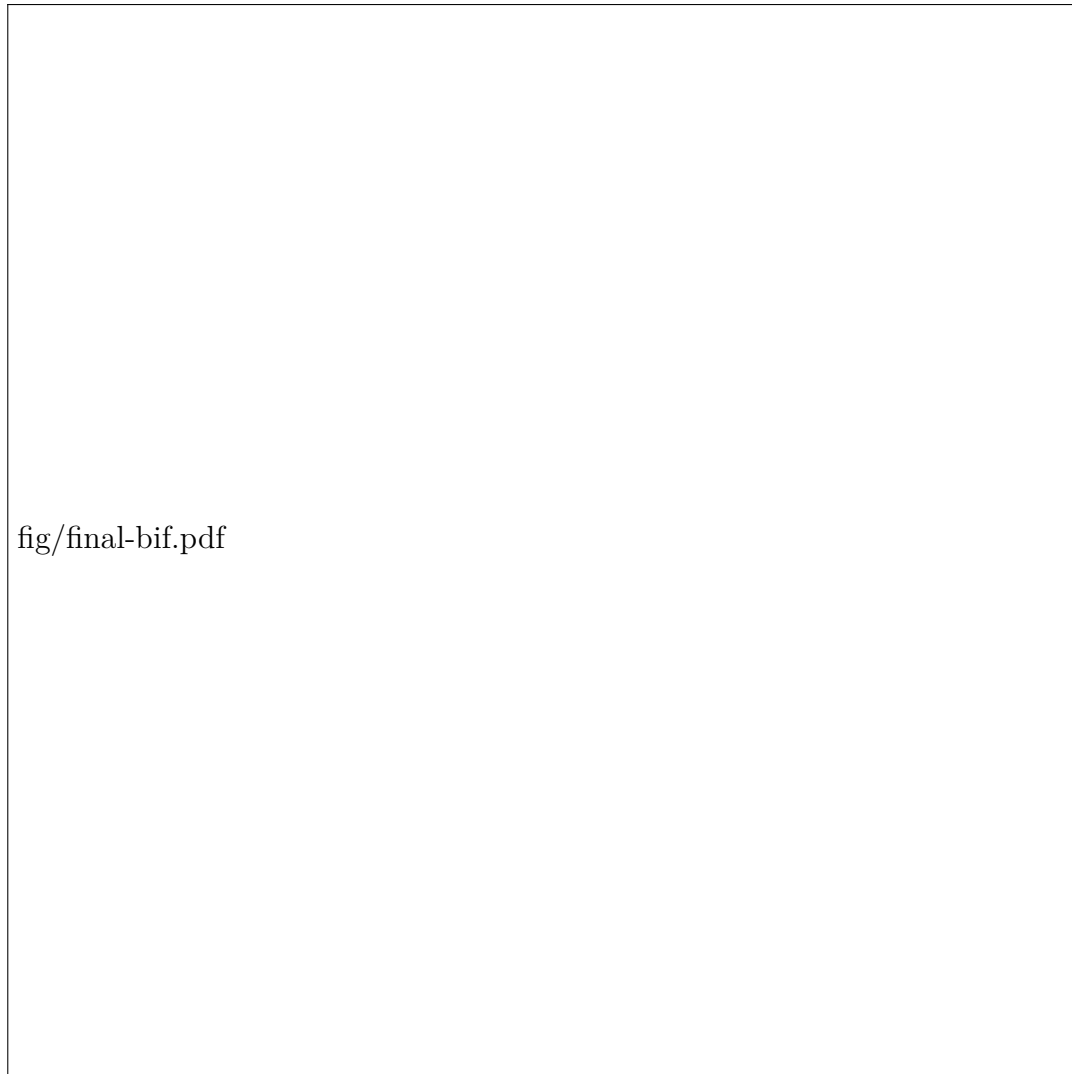
Figure 12. Bifurcation diagrams of stable $n : n$ solutions computed analytically from fixed points of Π_n and plotted on the respective intervals of $\bar{g} \in \left[\bar{g}_+(n), \bar{g}_-(n)\right]$ (blue), and computed from numerical integrations of the ODEs (orange).